photonics

MDPI

Article

Valley-Selective High Harmonic Generation and Polarization Induced by an Orthogonal Two-Color Laser Field

Xi Liu [1,2,*], Dongdong Liu [1,2], Yan Sun [1,2], Yujie Li [1] and Cui Zhang [1]

[1] School of Physics and New Energy, Xuzhou University of Technology, Xuzhou 221018, China
[2] State Key Laboratory of Millimeter Waves, Southeast University, Nanjing 210096, China
* Correspondence: liuxi@xzit.edu.cn

Abstract: The valley pseudospin properties of electrons in two-dimensional hexagonal materials result in many fascinating physical phenomena, which opens up the new field of valleytronics. The valley-contrasting physics aims at distinguishing the valley degree of freedom based on valley-dependent effects. Here, we theoretically demonstrate that both of the valley-selective high harmonic generation and valley-selective electronic excitation can be achieved by using an orthogonal two-color (OTC) laser field in gapped graphene. It is shown that the asymmetry degrees of harmonic yields in the plateaus, cutoff energies of generated harmonics and electron populations from two different valleys can be precisely controlled by the relative phase of the OTC laser field. Thus, the selectivity of the dominant valley for the harmonic radiation and electronic polarization can be switched by adjusting the relative phase of the OTC laser field. Our work offers an all-optical route to produce the valley-resolved high harmonic emissions and manipulate the ultrafast valley polarization on a femtosecond timescale in condensed matter.

Keywords: high harmonic generation; orthogonal two-color field; valleytronics; gapped graphene

Citation: Liu, X.; Liu, D.; Sun, Y.; Li, Y.; Zhang, C. Valley-Selective High Harmonic Generation and Polarization Induced by an Orthogonal Two-Color Laser Field. *Photonics* **2023**, *10*, 1126. https://doi.org/10.3390/photonics10101126

Received: 17 September 2023
Revised: 3 October 2023
Accepted: 6 October 2023
Published: 8 October 2023

1. Introduction

When matter is exposed to a strong laser field, some interesting light-induced phenomena will be observed due to the highly nonlinear processes [1–4]. In particular, high harmonic generation (HHG) is one of the most attractive subjects in strong-field physics and has been studied extensively in the past several decades [5–10]. In the HHG process, a fundamental frequency laser is converted into bursts of high-energy photons. Thus, the obtained harmonics enable the generation of coherent extreme ultraviolet or soft X-ray light sources [11–13]. HHG is typically activated in atomic or molecular gases. The experimental observation of high harmonic emissions from solids has aroused great interest in recent years [14–20]. High harmonic spectroscopy (HHS) in solids provides an efficient way to probe the electronic structures and ultrafast dynamics of solid targets, such as the reconstruction of band structures [21,22] and the detect of topological phase transitions [23–25] in materials. Specifically, the two-dimensional (2D) hexagonal crystals, such as the graphene and transition metal dichalcogenides (TMDs), have always been the quite suitable and fashionable target media for the HHG in solids because of their extraordinary transport properties. The characteristics of HHG from 2D hexagonal materials have been widely researched in both theory [26–28] and experiment [29–32].

The energy bands of 2D hexagonal crystals in Brillouin zone (BZ) contain two energy-degenerated and nonequivalent local extrema, which are called Dirac points and are denoted as K and K' [33,34]. The motions of charge carriers near the Dirac points are described by the massless Dirac equation, which brings in an extra electronic degree of freedom, called valley pseudospin. The magical properties of the valley pseudospin lead to lots of novel physical phenomena and open up the frontier of valleytronics [35–37]. Nowadays, how to effectively distinguish the valley degree of freedom by breaking the

symmetry between the K and K' valleys has become a popular research topic, namely, valley-contrasting physics [38]. Many valley asymmetry effects have been found in light-induced phenomena [39–44].

For a hexagonal lattice with broken inversion symmetry, the orbital magnetic moments of the two valleys are opposite due to the sign reversals of the non-vanishing Berry curvatures in the neighborhood of the K and K' valleys [38]. This fact gives rise to the valley optical selection rules [39–41]. That is, K and K' valleys are coupled exclusively to the left and right circularly polarized (CP) photons in direct interband transitions, respectively. The unique valley-selective circular dichroism (VSCD) promises that the valley selectivity of the electronic excitation can be controlled by using a bandgap-resonant CP pump laser with the matching helicity [45]. However, it is widely recognized that the linearly polarized (LP) light is unsuitable for the valley polarization because the LP laser field responds equally to two valleys [35–39]. Recently, Jiménez–Galán et al. [41] have offered an ingenious proposal to implement the valley polarization by using a few-cycle LP laser pulse with the controlled carrier-envelope phase (CEP). In addition, the valley selectivity of the HHG has also been achieved via the counter-rotating bicircular (CRB) laser field in latest studies [46–49].

In this work, we propose a general scheme to generate the valley-selective high harmonic radiation and electronic polarization using an orthogonal two-color (OTC) laser field in gapped graphene. Our results suggest that the relative magnitudes of harmonic yields in plateaus, cutoff energies of emitted harmonics and excitation probabilities contributed by K and K' valleys can be accurately regulated by the relative phase of the OTC laser field. The controlled asymmetries between two different valleys can serve as a promising tool for achieving the ultrafast valley switching in the intense laser field.

2. Theoretical Models

In our simulations, the gapped graphene is imitated by a 2D two-band model with the tight-binding approximation [33,50]. Herein, only the p_z orbitals are considered at each atomic site for the sake of simplicity. Atomic units are used throughout this paper unless otherwise stated. The lattice constant of the gapped graphene is chosen as $a = 2.46$ Å [46]. In this model, analytical expressions of physical quantities involving electronic structures can be derived [51–54]. The dispersion relations of the conduction band (CB) and valence band (VB) in the gapped graphene can be expressed as

$$E_{\mathrm{m}} = \pm\sqrt{\gamma^2|f(\mathbf{k})|^2 + \left(\frac{\Delta}{2}\right)^2}, \tag{1}$$

where the band subscript $\mathrm{m} = (\mathrm{c}, \mathrm{v})$ stands for the CB and VB, respectively. $\mathbf{k} = (k_x, k_y)$ is the wave vector of the Bloch electrons in k-space. In Equation (1), the positive and negative signs correspond to the CB and VB, respectively. γ is the transfer energy of the nearest-neighbor hopping and is chosen as 3.03 eV [51]. Δ is the energy gap between the CB and VB at Dirac points and is given by $\Delta = 1$ eV in the model. For the gapped graphene, the inversion symmetry is broken due to the nonzero bandgap Δ. $f(\mathbf{k})$ is represented as

$$f(\mathbf{k}) = \exp\left(\mathrm{i}\frac{a}{\sqrt{3}}k_x\right) + 2\exp\left(-\mathrm{i}\frac{a}{2\sqrt{3}}k_x\right)\cos\left(\frac{a}{2}k_y\right). \tag{2}$$

Thus, the modulus of $f(\mathbf{k})$ is calculated by

$$|f(\mathbf{k})| = \sqrt{1 + 4\cos\left(\frac{\sqrt{3}a}{2}k_x\right)\cos\left(\frac{a}{2}k_y\right) + 4\cos^2\left(\frac{a}{2}k_y\right)}. \tag{3}$$

The transition dipole moment (TDM) of the gapped graphene is obtained as [51,52]

$$\mathbf{d}(\mathbf{k}) = -\frac{\gamma|f(\mathbf{k})|}{2E_c(\mathbf{k})}\nabla_{\mathbf{k}}\phi(\mathbf{k}) + \mathrm{i}\frac{\gamma\Delta}{4E_c^2(\mathbf{k})}\nabla_{\mathbf{k}}|f(\mathbf{k})|, \tag{4}$$

where $\phi(\mathbf{k}) = \mathrm{Arg}[f(\mathbf{k})]$. Figure 1a shows the calculated band structures of the CB and VB for the gapped graphene, where six Dirac cones are presented in k-space. The energy band of the VB is depicted individually using a 2D pseudocolor diagram to clearly display the K and K' valleys in Figure 1b.

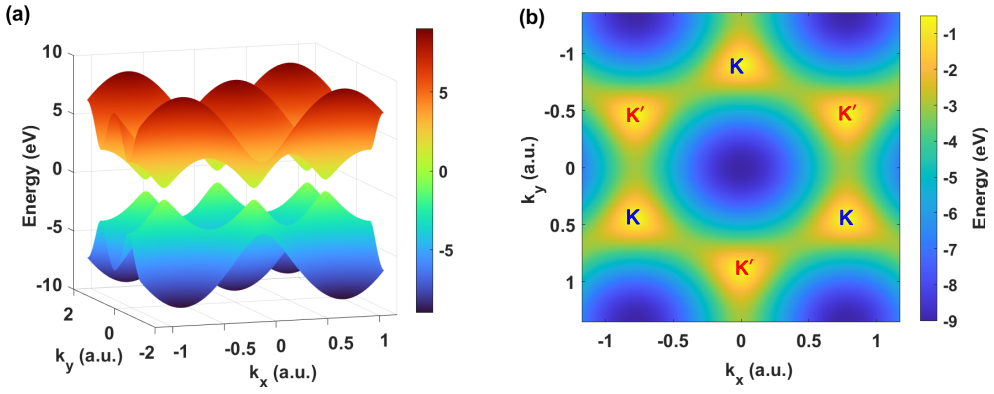

Figure 1. (**a**) Band structures of the CB and VB for the gapped graphene with a bandgap $\Delta = 1$ eV. (**b**) K and K' valleys in the VB.

The interaction of an intense laser field and target material is described by the 2D two–band density matrix equations (DMEs) [55–58] :

$$\dot{\pi}(\mathbf{K},t) = -\mathrm{i}\Omega(\mathbf{K},t)w(\mathbf{K},t)\mathrm{e}^{-\mathrm{i}S(\mathbf{K},t)} - \frac{\pi(\mathbf{K},t)}{T_2}, \tag{5}$$

$$\dot{n}_{\mathrm{v}}(\mathbf{K},t) = -\mathrm{i}\Omega^*(\mathbf{K},t)\pi(\mathbf{K},t)\mathrm{e}^{\mathrm{i}S(\mathbf{K},t)} + \mathrm{c.c.}, \tag{6}$$

$$\dot{n}_{\mathrm{c}}(\mathbf{K},t) = \mathrm{i}\Omega^*(\mathbf{K},t)\pi(\mathbf{K},t)\mathrm{e}^{\mathrm{i}S(\mathbf{K},t)} + \mathrm{c.c.}, \tag{7}$$

where n_{v} and n_{c} are the crystal-momentum-resolved populations of the VB and CB, respectively. $w = n_{\mathrm{v}} - n_{\mathrm{c}}$ is the population difference between the VB and CB. $\pi(\mathbf{K},t)$ is the off-diagonal element of the density matrix. The classical action with vector potential $\mathbf{A}(t)$ is given by $S(\mathbf{K},t) = \int_{-\infty}^{t}\varepsilon_{\mathrm{g}}[\mathbf{K}+\mathbf{A}(\tau)]\mathrm{d}\tau$, where $\varepsilon_{\mathrm{g}} = E_{\mathrm{c}} - E_{\mathrm{v}}$ is the bandgap between the CB and VB. Ω is the Rabi frequency and is written as $\Omega(\mathbf{K},t) = \mathbf{F}(t)\cdot\mathbf{d}[\mathbf{K}+\mathbf{A}(t)]$, where $\mathbf{F}(t) = -\mathrm{d}\mathbf{A}/\mathrm{d}t$ is the laser field. T_2 is the dephasing time accounting for the decoherence effect in solids. In the strong laser field, the light-induced excitations occur mainly in the vicinity of Dirac points because the energy difference between the CB and VB reaches the minimum here. Hence, valence electrons in VB are initially occupied within the circular areas centered at the Dirac points in our calculations. The radius of the circular area is chosen as $0.1k_D$, where $k_D = 4\pi/(3a)$ is the distance between two adjacent Dirac points in the reciprocal space. It is noted that the multiple-plateau structures will appear in HHG spectra if the higher CBs are considered in our model. This is because the electronic transitions from the first and higher-lying CBs to the VB result in the primary and latter plateaus in HHG spectra, respectively, as pointed out in previous studies [17–19]. The crossings of energy bands will give rise to the merging of neighboring harmonic plateaus [19]. In our calculations, we only focus on the primary plateaus of the HHG spectra because the intensities of higher plateaus are much weaker than those of the primary plateaus.

We adopt an OTC laser field polarized in the $x-y$ plane. The OTC laser pulse is composed of two mutually orthogonal LP laser fields with the fundamental frequency and

its second harmonic. In our calculations, the ratio of strengths for the two LP fields is 1:1. The OTC laser field reads as

$$\mathbf{F}(t) = f(t)F_0\left[\cos(\omega t)\hat{\mathbf{e}}_x + \cos(2\omega t + \varphi)\hat{\mathbf{e}}_y\right], \tag{8}$$

where ω is the fundamental frequency of the laser field, F_0 is the amplitude of the laser field, and $f(t)$ is the envelope of the laser pulse. $\hat{\mathbf{e}}_x$ and $\hat{\mathbf{e}}_y$ are the unit vectors of x and y axes, respectively. φ is the relative phase of the two LP laser fields. The wavelength of the fundamental laser field is 3200 nm. The laser intensity is 6×10^{11} W/cm^2 for both of the two LP laser fields in all calculations. Sine-squared envelope is adopted with a total duration of $8T_0$, where T_0 is the duration of one optical cycle of the fundamental laser field. The dephasing time is chosen as $T_2 = 0.2T_0$ in our calculation.

The total laser-induced current $\mathbf{j}$ in solids is divided into the intraband current $\mathbf{j}_{\mathrm{ra}}$ and interband current $\mathbf{j}_{\mathrm{er}}$, i.e.,

$$\mathbf{j} = \mathbf{j}_{\mathrm{ra}} + \mathbf{j}_{\mathrm{er}}. \tag{9}$$

The intraband and interband currents are calculated by [55]

$$\mathbf{j}_{\mathrm{ra}}(t) = \sum_{\mathrm{m=c,v}} \int_{\mathrm{BZ}} \mathbf{v}_{\mathrm{m}}[\mathbf{K} + \mathbf{A}(t)] n_{\mathrm{m}}(\mathbf{K}, t) \mathrm{d}^2\mathbf{K}, \tag{10}$$

$$\mathbf{j}_{\mathrm{er}}(t) = \frac{\mathrm{d}}{\mathrm{d}t} \int_{\mathrm{BZ}} \mathbf{p}(\mathbf{K}, t) \mathrm{d}^2\mathbf{K}, \tag{11}$$

respectively, where $\mathbf{v}_{\mathrm{m}}(\mathbf{k}) = \nabla_{\mathbf{k}} E_{\mathrm{m}}(\mathbf{k})$ is the band velocity, and $\mathbf{p}(\mathbf{K}, t)$ is given by

$$\mathbf{p}(\mathbf{K}, t) = \mathbf{d}[\mathbf{K} + \mathbf{A}(t)] \pi(\mathbf{K}, t) \mathrm{e}^{\mathrm{i}S(\mathbf{K}, t)} + \mathrm{c.c.} \tag{12}$$

The high harmonic yield is calculated by the Fourier transform of the total current $\mathbf{j}$:

$$H(\omega) = \left| \int \mathbf{j}(t) \mathrm{e}^{\mathrm{i}\omega t} \mathrm{d}t \right|^2. \tag{13}$$

A Hanning window [59–61] is used before the Fourier transformation to improve the signal-to-noise ratio of generated harmonic signals. The time-dependent electron population in the CB is obtained as

$$N_{\mathrm{c}}(t) = \int_{\mathrm{BZ}} n_{\mathrm{c}}(\mathbf{K}, t) \mathrm{d}^2\mathbf{K}. \tag{14}$$

3. Results and Discussion

High harmonic spectra contributed by the K and K' valleys are calculated selectively by assuming that valence electrons are initially occupied in the vicinity of two different valleys. By evolving the coupled DMEs over time t under the OTC laser fields with various relative phases φ according to Equations (5)–(7), the light-induced total current $\mathbf{j}(t)$ can be calculated by Equations (9)–(12). Finally, high harmonic spectra are obtained by the Fourier transform of $\mathbf{j}(t)$ using Equation (13). Experimentally, the bandgap Δ in graphene can be induced by growing graphene on a SiC substrate [62], or by designing a heterostructure of graphene with hexagonal boron nitride (BN) [63], or by putting strain on graphene [64]. The second harmonic of the OTC laser field can be achieved via a beta–barium–borate (BBO) crystal. The relative phase of the OTC laser field can be continuously adjusted by rotating a fused-silica plate, which is placed behind the BBO crystal. This optical setup is similar to that employed by Brugnera et al. [65]. The generated HHG signals can be collected by a spectrometer equipped with a thermoelectrically cooled Si charge-coupled device (CCD) camera.

Figure 2a–d show the obtained valley-resolved harmonic spectra with $\varphi = 0°$, $90°$, $180°$, and $270°$, respectively. Herein, the observed odd-order harmonics are LP along the x direction, whereas the even-order harmonics are LP along the y direction. In our

calculations, it is found that the obtained harmonics contributed by intraband currents contain both odd and even orders. However, obtained harmonics arising from interband transitions contain only odd orders. Therefore, even-order harmonics in the plateau are absent in observed harmonic spectra, because intraband and interband harmonics are, respectively, dominant in the below-band-gap regions and harmonic plateau as pointed in previous studies [19,55,61]. In fact, the allowed harmonic orders in the observed overall HHG spectrum essentially are determined by the dynamical symmetry of the gapped graphene and the OTC laser field. The destructive interferences of the light-induced currents between the K and K' valleys lead to the vanishing of forbidden harmonic orders in overall HHG spectra.

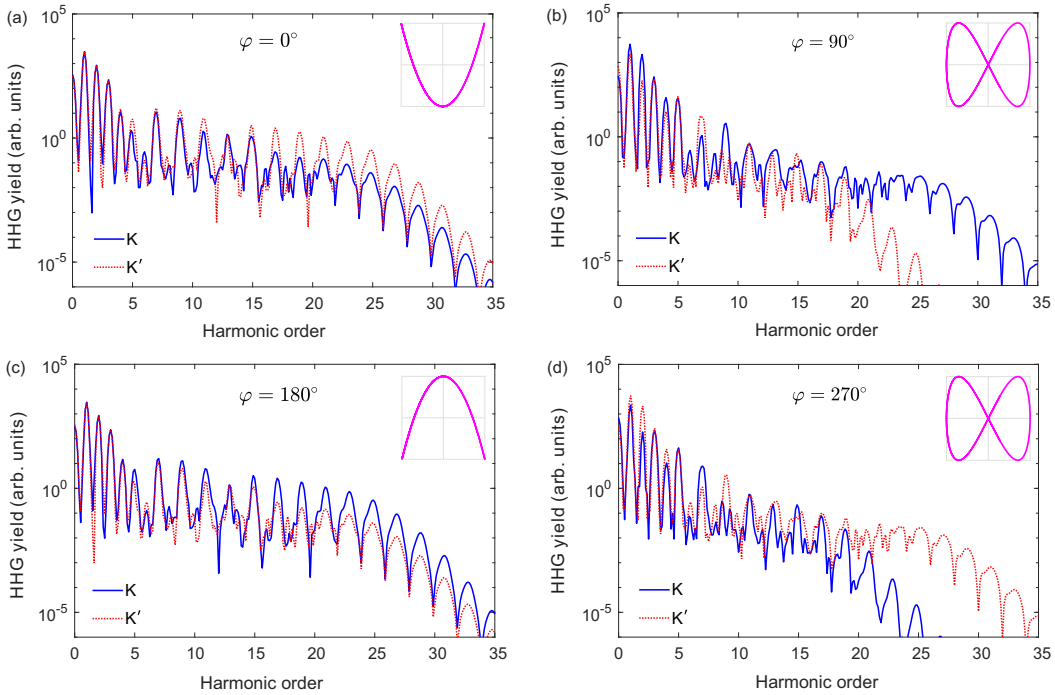

Figure 2. High harmonic spectra from the K and K' valleys with various relative phases of OTC laser fields: (**a**) $\varphi = 0°$, (**b**) $\varphi = 90°$, (**c**) $\varphi = 180°$, and (**d**) $\varphi = 270°$. The Lissajous figures of the laser fields are plotted in the insets at the upper-right corners of the panels.

Significant valley–discriminating harmonic signals can be observed in Figure 2a–d. As shown in Figure 2a, one can see clearly that the intensities of harmonics from the K' valley are about one order of magnitude higher than those from the K valley in the plateau region when $\varphi = 0°$. Thus, the observed overall harmonics in plateau are dominated by the contributions from the K' valley in this case. When φ is chosen as 180°, the relative intensities of harmonics in plateaus from two different valleys are exactly reversed compared to the case of $\varphi = 0°$. As shown in Figure 2c, the yields of harmonics in plateau from the K' valley are about one order of magnitude lower than those from the K valley when $\varphi = 180°$. Then the harmonics contributed by the K valley are dominant in plateau region for the observed overall harmonics. Furthermore, the intensities of harmonic plateaus from two different valleys become approximately equal in magnitude when φ is chosen as 90° or 270° as presented in Figure 2b,d. Herein, the generated harmonics in plateau are contributed equally to the K and K' valleys. Our results suggest that the relative yields of harmonic plateaus from the K and K' valleys can be effectively controlled by the relative phase of the OTC laser field, which is significant for achieving valley-selective HHG from solids. In fact, the unequal responses of two different valleys in the HHG processes originate from the asymmetries of OTC laser fields in real space. Specifically, the Lissajous figures always preserve the inversion symmetry in x direction for arbitrary φ as shown in the insets in Figure 2a–d. However, the inversion symmetries of Lissajous figures in y direction are

broken except for the cases of $\varphi = 90°$ and $\varphi = 270°$. The light-induced valley asymmetry in y direction for the HHG process leads to the valley-resolved HHG, such as the cases of $\varphi = 0°$ and $\varphi = 180°$ shown in Figure 2a,c, respectively.

In order to demonstrate the valley manipulation of the HHG in gapped graphene, the dependence of harmonic yields in plateau from two different valleys on φ is further investigated in our studies. The 15th-order harmonic (denoted as H_{15}) is chosen as the representative of obtained harmonics in plateau. Figure 3a shows the harmonic yields of H_{15} from the K and K' valleys as a function of φ in polar coordinates. The significantly distinguishable harmonic yields from the two valleys can be observed in certain intervals of φ. Specifically, the harmonic yield from the K' valley is overwhelming with φ ranging from $-30°$ to $60°$, whereas the harmonic yield from the K valley is distinctively predominant when φ is located at the interval ranging from $150°$ to $240°$ as shown in Figure 3a. The harmonic yields from two different valleys are comparable in other intervals of φ. We also calculate the average yield between 11th–order and 19th–order harmonics (denoted as H_{avg}) to evaluate the harmonic efficiency in plateau. Figure 3b shows H_{avg} contributed by the K and K' valleys as a function of φ in polar coordinates. One can see clearly that H_{avg} is prominently dominated by the K' and K valleys in the relative phase interval ranging from $-60°$ to $60°$ and that ranging from $120°$ to $240°$, respectively. The valley-resolved harmonic yields in plateau with various φ are clearly presented in Figure 3a,b as the above discussion.

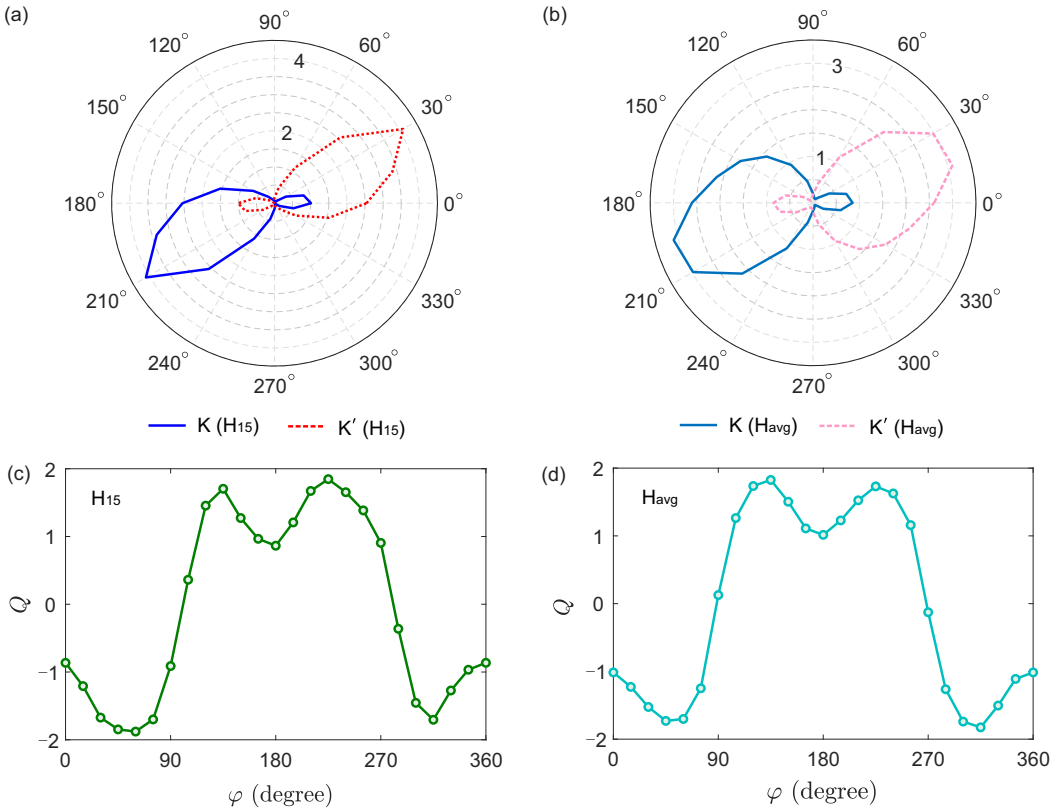

Figure 3. High harmonic yields from the K and K' valleys as a function of relative phase φ of the OTC laser field for (**a**) H_{15} and (**b**) H_{avg}. Valley deviation parameter Q as a function of φ for (**c**) H_{15} and (**d**) H_{avg}. H_{15} denotes the 15th-order harmonic. H_{avg} denotes the average yield of harmonics in plateau, which is calculated as the average yield between 11th-order and 19th-order harmonics.

To quantitatively evaluate the asymmetry degree of the harmonic yield between the two different valleys, we calculate the valley deviation parameter Q defined as [46,66–68]

$$Q = \frac{H_K - H_{K'}}{(H_K + H_{K'})/2'} \tag{15}$$

where H_K and $H_{K'}$ are the obtained harmonic yields from the K and K' valleys, respectively. Figure 3c,d show the calculated Q as a function of φ for H_{15} and H_{avg}, respectively. It turns out that the valley asymmetry of the HHG in plateau region can be regulated precisely by the relative phase φ. From Figure 3c,d, it is found that the valley deviation of the harmonic yield in plateau is close to 0 when φ is approximately equal to 90° or 270°, which corresponds to the results shown in Figure 2b,d. On the contrary, the valley asymmetries of harmonic plateaus between K' and K valleys reach maximum when φ is close to $\pm 45°$ and $180° \pm 45°$, respectively. Our results suggest that the relative contribution of the two different valley for the HHG in plateau can be well controlled via φ. This feature guarantees the capability of generating and controlling the valley-selective HHG in gapped graphene.

Apart from the harmonic yield in plateau, the valley asymmetry of the harmonic cutoff is also found in our studies. The cutoff orders of generated harmonics from the K and K' valleys as a function of φ are shown in Figure 4a in polar coordinates. Here, the observed cutoff orders of harmonics from two valleys exhibit the obvious difference for the various φ except for the case of $\varphi = 0°$ and 180°. From Figure 4a, one can see that the harmonic cutoff from the K valley is greater that from the K' valley when φ varies from 0° to 180°, whereas the relativeness is reversed when φ belongs to the interval ranging from 180° to 360°. It is noticed that the Lissajous figure of the OTC laser field exhibits a bivalve structure containing the left and right lobes when $\varphi \neq 0°$ or 180°. We find that the valley selectivity of the harmonic cutoff is associated with the helicity of the left/right lobe of the OCT laser field. Specifically, the left lobe of the OTC laser field rotates in an anticlockwise direction and the right lobe of that rotates in a clockwise direction when φ ranges from 0° to 180°. However, the helicities of both two lobes reverse when φ is located at the interval ranging from 180° to 360°. The rotation directions and helicity configurations of the OTC laser fields for $\varphi = 90°$ and 270° are chosen as the examples and are shown in Figure 4b. The asymmetric couplings of the two different valleys to the specific helicity of the OCT laser field result in the valley discrimination of the harmonic cutoff.

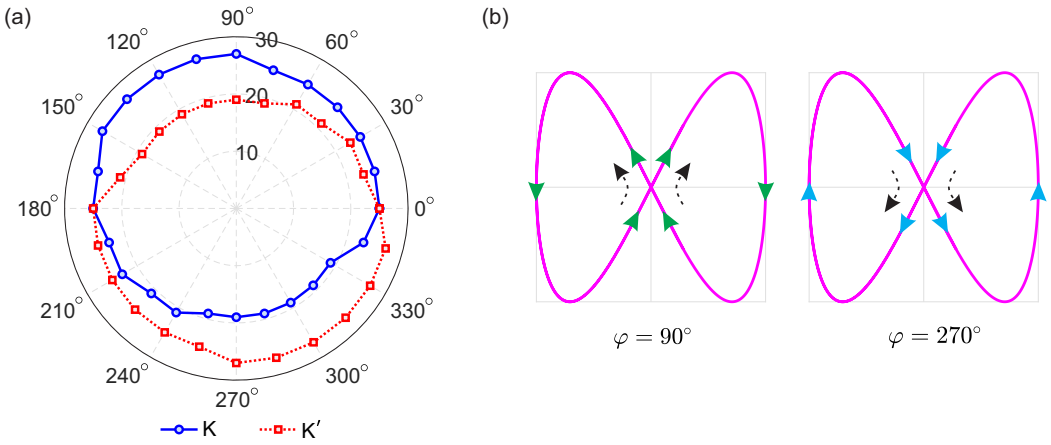

Figure 4. (**a**) Cutoff orders of harmonics contributed by the K and K' valleys as a function of φ. (**b**) The Lissajous figures of adopted OTC laser fields with $\varphi = 90°$ and 270°. The solid arrow indicates the rotation direction of the laser field. The dashed arrow indicates the helicity of the left/right lobe of the OTC laser field.

The substantial contrast between the two valleys for the electronic excitation can also be obtained via the OTC laser field in our scheme. Figure 5a–h show the time-dependent electron populations of the CB from K and K' valleys with $\varphi = 0°$, 45°, 90°, 135°, 180°, 225°, 270° and 315°, respectively. From Figure 5a–h, one can see clearly that N_c is almost exactly the same when $\varphi = 0°$ or 180°, whereas remarkable divergences of N_c are present for the other cases. As shown in Figure 5b–d, the electronic excitation from the K' valley is distinctly superior to that from the K valley when $\varphi = 45°$, 90° and 135°. In particular, the electron population at the end of the laser pulse from the K' valley is nearly twice as much

as that from the K valley when $\varphi = 90°$ as shown in Figure 5c. On the contrary, the relative magnitudes of electronic excitations from two valleys are exactly reversed when $\varphi = 225°$, 270° and 315° as presented in Figure 5f–h. In these cases, the K valley is dominant for the processes of electronic excitations in gapped graphene. The valley asymmetry of the electronic excitation induced by the OTC laser field offers a useful way to achieve the valley polarization using the LP laser pulse. Compared with a traditional method via the bandgap-resonant CP laser pulse based on the valley optical selection rules, our scheme, performed with non-resonant LP laser pulses, has the advantages of better accessibility and flexibility.

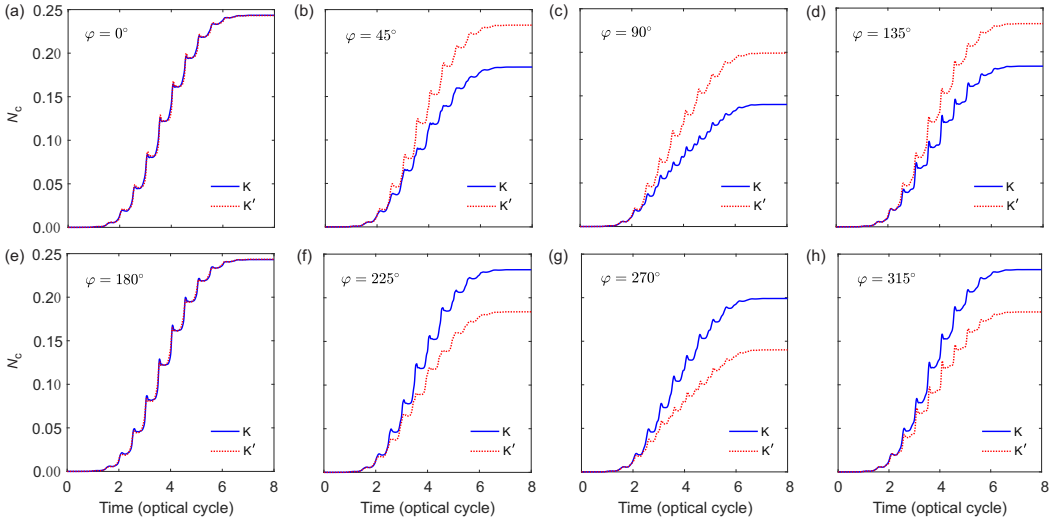

Figure 5. The time–dependent electron populations N_c from K and K' valleys with various relative phases of OTC laser fields: (**a**) $\varphi = 0°$, (**b**) $\varphi = 45°$, (**c**) $\varphi = 90°$, (**d**) $\varphi = 135°$, (**e**) $\varphi = 180°$, (**f**) $\varphi = 225°$, (**g**) $\varphi = 270°$, and (**h**) $\varphi = 315°$.

Our research further suggests that the degree of the valley polarization can be precisely controlled by the relative phase of the OTC laser field. Figure 6a shows the electron populations at the end of the laser pulse from two valleys as a function of φ for the CB. This result indicates that the asymmetry degree of the electron populations between two different valleys changes simultaneously with φ. Thus, the dominant valley for the electronic polarization can be shifted by choosing given φ. As shown in Figure 6a, the valley polarization always occurs for various φ except for the cases of $\varphi = 0°$ and 180°. The K' and K are prevailing for the valley polarization with φ belonging to the interval ranging from 0° to 180° and that ranging from 180° to 360°, respectively. It is worth noting that the dependence of the electron population from two valleys on φ is highly similar to that of the harmonic cutoff shown in Figure 4a. Hence, the valley polarization induced by the OTC laser field can also be attributed to the asymmetric responses of two valleys to the helicities of two lobes of the OTC laser field. In order to quantify the degree of valley polarization, valley asymmetry parameter η is introduced and is defined as [46,66–68]

$$\eta = \frac{N_c^K - N_c^{K'}}{\left(N_c^K + N_c^{K'}\right)/2}, \tag{16}$$

where N_c^K and $N_c^{K'}$ are the electron populations at the end of the laser pulse from K and K' valleys in CB, respectively. The obtained values of η as a function of φ is shown in Figure 6b. One can see that the curve of η exhibits a typical fluctuation like a negative sinusoidal waveform. Herein, the valley polarization reaches the global maximum when $\varphi = 90°$ or 270°, where values of η are as high as $\pm 34.8\%$. The valley asymmetry of the electron population vanishes when $\varphi = 0°$ or 180°. The canonical modulation curve of η

on φ provides a solid foundation for manipulating the valley polarization accurately by varying the relative phase of the OTC laser field.

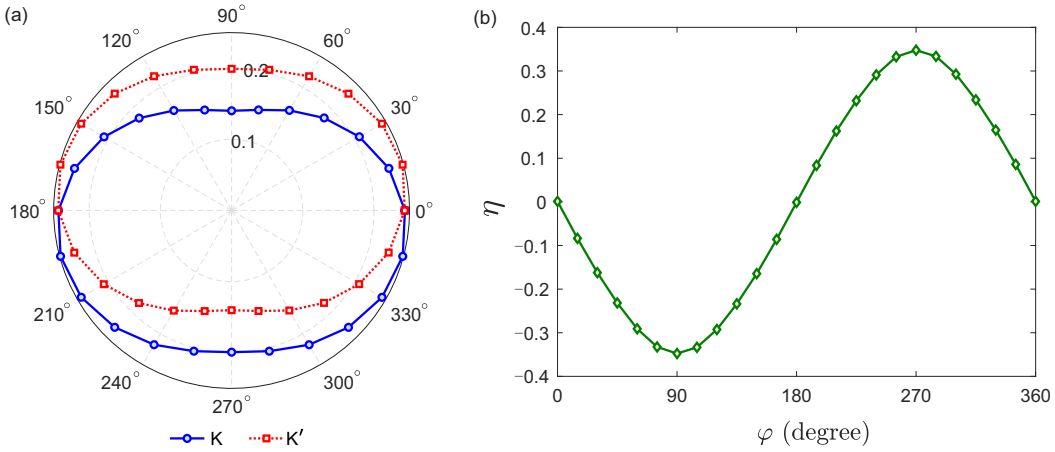

Figure 6. (**a**) The electron populations at the end of the laser pulse from K and K' valleys as a function of φ for the CB. (**b**) Valley asymmetry parameter η as a function of φ for the CB.

4. Conclusions

In summary, we theoretically investigate the contributions from K and K' valleys in the responses of the HHG and electronic excitation induced by the OTC laser field in gapped graphene. It is concluded that the asymmetry degrees of the harmonic yield in plateau, the harmonic cutoff and electron population between two different valleys are precisely controlled by the relative phase of the OTC laser field. The relative-phase-dependent valley asymmetries permit that the valley-selective HHG and electronic polarization can be achieved by choosing an applicable relative phase of the OTC laser field. Our scheme has the outstanding advantage of better manipulability and accessibility due to the usage of non-resonant LP laser pulses. This work opens an all-optical way to realize and control the valley asymmetry on a femtosecond timescale, which facilitates our understanding of ultrafast electron dynamics near Dirac points in valleytronic materials.

Author Contributions: Conceptualization, X.L.; methodology, X.L.; software, X.L.; validation, X.L., D.L. and Y.S.; formal analysis, X.L., D.L. and Y.S.; investigation, X.L. and Y.L.; resources, X.L.; data curation, X.L. and C.Z.; writing—original draft preparation, X.L.; writing—review and editing, X.L. and C.Z.; visualization, X.L. and C.Z.; supervision, X.L.; project administration, X.L.; funding acquisition, X.L. All authors have read and agreed to the published version of the manuscript.

Funding: This research was funded by the National Natural Science Foundation of China under Grants No. 12004325, Six Talent Peaks Project of Jiangsu Province of China under Grant No. JY–105 and State Key Laboratory Open Fund of Millimeter Waves under Grant No. K202105. Dongdong Liu was supported by the Jiangsu Qinglan project.

Institutional Review Board Statement: Not applicable.

Informed Consent Statement: Not applicable.

Data Availability Statement: The data supporting the findings of this study are available from the corresponding author upon reasonable request.

Conflicts of Interest: The authors declare no conflict of interest.

References

1. Krausz, F.; Ivanov, M. Attosecond physics. *Rev. Mod. Phys.* **2009**, *81*, 163.
2. Corkum, P.B.; Krausz, F. Attosecond science. *Nat. Phys.* **2007**, *3*, 381–387.
3. Hentschel, M.; Kienberger, R.; Spielmann, C.; Reider, G.A.; Milosevic, N.; Brabec, T.; Corkum, P.; Heinzmann, U.; Drescher, M.; Krausz, F. Attosecond metrology. *Nature* **2001**, *414*, 509–513. [PubMed]

4. Zhu, X.; Lu, P.; Lein, M. Control of the Geometric Phase and Nonequivalence between Geometric–Phase Definitions in the Adiabatic Limit. *Phys. Rev. Lett.* **2022**, *128*, 030401. [PubMed]
5. Schafer, K.J.; Yang, B.; DiMauro, L.F.; Kulander, K.C. Above threshold ionization beyond the high harmonic cutoff. *Phys. Rev. Lett.* **1993**, *70*, 1599.
6. Corkum, P.B. Plasma perspective on strong field multiphoton ionization. *Phys. Rev. Lett.* **1993**, *71*, 1994. [CrossRef]
7. Lewenstein, M.; Balcou, P.; Ivanov, M.Y.; L'Huillier, A.; Corkum, P.B. Theory of high-harmonic generation by low–frequency laser fields. *Phys. Rev. A* **1994**, *49*, 2117. [PubMed]
8. He, L.; Lan, P.; Le, A.; Wang, B.; Wang, B.; Zhu, X.; Lu, P.; Lin, C.D. Real–Time Observation of Molecular Spinning with Angular High–Harmonic Spectroscopy. *Phys. Rev. Lett.* **2018**, *121*, 163201. [PubMed]
9. Ganeev, R.A. High–Order Harmonics Generation in Selenium–Containing Plasmas. *Photonics* **2023**, *10*, 854.
10. Liu, X.; Zhu, X.; Li, L.; Li, Y.; Zhang, Q.; Lan, P.; Lu, P. Selection rules of high–order–harmonic generation: Symmetries of molecules and laser fields. *Phys. Rev. A* **2016**, *94*, 033410.
11. Paul, P.M.; Toma, E.S.; Breger, P.; Mullot, G.; Augé, F.; Balcou, P.; Muller, H.G.; Agostini, P. Observation of a Train of Attosecond Pulses from High Harmonic Generation. *Science* **2001**, *292*, 1689–1692.
12. Chatziathanasiou, S.; Kahaly, S.; Skantzakis, E.; Sansone, G.; Lopez-Martens, R.; Haessler, S.; Varju, K.; Tsakiris, G.D.; Charalambidis, D.; Tzallas, P. Generation of Attosecond Light Pulses from Gas and Solid State Media. *Photonics* **2017**, *4*, 26.
13. Zhai, C.; Zhu, X.; Long, J.; Shao, R.; Zhang, Y.; He, L.; Tang, Q.; Li, Y.; Lan, P.; Yu, B.; et al. Generation of elliptically polarized attosecond pulses in mixed gases. *Phys. Rev. A* **2021**, *103*, 033114.
14. Ghimire, S.; DiChiara, A.D.; Sistrunk, E.; Agostini, P.; DiMauro, L.F.; Reis, D.A. Observation of high–order harmonic generation in a bulk crystal. *Nat. Phys.* **2011**, *7*, 138–141.
15. Kruchinin, S.Y.; Krausz, F.; Yakovlev, V.S. Colloquium: Strong–field phenomena in periodic systems. *Rev. Mod. Phys.* **2018**, *90*, 021002.
16. Han, S. High–Harmonic Generation Using a Single Dielectric Nanostructure. *Photonics* **2022**, *9*, 427.
17. Vampa, G.; Hammond, T.J.; Thiré, N.; Schmidt, B.E.; Légaré, F.; McDonald, C.R.; Brabec, T.; Corkum, P.B. Linking high harmonics from gases and solids. *Nature* **2015**, *522*, 462–464.
18. Wu, M.; Browne, D.A.; Schafer, K.J.; Gaarde, M.B. Multilevel perspective on high-order harmonic generation in solids. *Phys. Rev. A* **2016**, *94*, 063403.
19. Liu, X.; Zhu, X.; Lan, P.; Zhang, X.; Wang, D.; Zhang, Q.; Lu, P. Time–dependent population imaging for high–order–harmonic generation in solids. *Phys. Rev. A* **2017**, *95*, 063419.
20. Fu, S.; Feng, Y.; Li, J.; Yue, S.; Zhang, X.; Hu, B.; Du, H. Recollision dynamics analysis of high–order harmonic generation in solids. *Phys. Rev. A* **2020**, *101*, 023402.
21. Lanin, A.A.; Stepanov, E.A.; Fedotov, A.B.; Zheltikov, A.M. Mapping the electron band structure by intraband high–harmonic generation in solids. *Optica* **2017**, *4*, 516–519.
22. Li, L.; Lan, P.; He, L.; Cao, W.; Zhang, Q.; Lu, P. Determination of Electron Band Structure using Temporal Interferometry. *Phys. Rev. Lett.* **2020**, *124*, 157403.
23. Bauer, D.; Hansen, K.K. High–Harmonic Generation in Solids with and without Topological Edge States. *Phys. Rev. Lett.* **2018**, *120*, 177401. [PubMed]
24. Heide, C.; Kobayashi, Y.; Baykusheva, D.R.; Jain, D.; Sobota, J.A.; Hashimoto, M.; Kirchmann, P.S.; Oh, S.; Heinz, T.F.; Reis, D.A.; et al. Probing topological phase transitions using high-harmonic generation. *Nat. Photon.* **2022**, *16*, 620–624.
25. Schmid, C.P.; Weigl, L.; Grössing, P.; Junk, V.; Gorini, C.; Schlauderer, S.; Ito, S.; Meierhofer, M.; Hofmann, N.; Afanasiev, D.; et al. Tunable non-integer high-harmonic generation in a topological insulator. *Nature* **2021**, *593*, 385–390. [PubMed]
26. Yue, L.; Hollinger, R.; Uzundal, C.B.; Nebgen, B.; Gan, Z.; Najafidehaghani, E.; George, A.; Spielmann, C.; Kartashov, D.; Turchanin, A.; et al. Signatures of Multiband Effects in High–Harmonic Generation in Monolayer MoS_2. *Phys. Rev. Lett.* **2022**, *129*, 147401.
27. Tamaya, T.; Akiyama, H.; Kato, T. Shear-strain controlled high-harmonic generation in graphene. *Phys. Rev. B* **2023**, *107*, L081405.
28. Rana, N.; Mrudul, M.S.; Kartashov, D.; Ivanov, M.; Dixit, G. High-harmonic spectroscopy of coherent lattice dynamics in graphene. *Phys. Rev. B* **2022**, *106*, 064303.
29. Yoshikawa, N.; Tamaya, T.; Tanaka, K. High-harmonic generation in graphene enhanced by elliptically polarized light excitation. *Science* **2017**, *356*, 736–738. [PubMed]
30. Heide, C.; Kobayashi, Y.; Johnson, A.C.; Liu, F.; Heinz, T.F.; Reis, D.A.; Ghimire, S. Probing electron–hole coherence in strongly driven 2D materials using high–harmonic generation. *Optica* **2022**, *9*, 512–516.
31. Cha, S.; Kim, M.; Kim, Y.; Choi, S.; Kang, S.; Kim, H.; Yoon, S.; Moon, G.; Kim, T.; Lee, Y.W.; et al. Gate–tunable quantum pathways of high harmonic generation in graphene. *Nat. Commun.* **2022**, *13*, 6630. [PubMed]
32. Zheng, W.; Jiang, Y.; Wang, S.; Liu, C.; Bai, Y.; Liu, P.; Li, R. Frequency shift of even–order high harmonic generation in monolayer MoS_2. *Opt. Express* **2023**, *31*, 27029–27040.
33. Castro Neto, A.H.; Guinea, F.; Peres, N.M.R.; Novoselov, K.S.; Geim, A.K. The electronic properties of graphene. *Rev. Mod. Phys.* **2009**, *81*, 109.
34. Geim, A.K. Graphene: Status and Prospects. *Science* **2009**, *324*, 1530–1534.

35. Schaibley, J.R.; Yu, H.; Clark, G.; Rivera, P.; Ross, J.S.; Seyler, K.L.; Yao, W.; Xu, X. Valleytronics in 2D materials. *Nat. Rev. Mater.* **2016**, *1*, 16055.
36. Vitale, S.A.; Nezich, D.; Varghese, J.O.; Kim, P.; Gedik, N.; Jarillo–Herrero, P.; Xiao, D.; Rothschild, M. Valleytronics: Opportunities, Challenges, and Paths Forward. *Small* **2018**, *14*, 1801483.
37. Langer, F.; Schmid, C.P.; Schlauderer, S.; Gmitra, M.; Fabian, J.; Nagler, P.; Schüller, C.; Korn, T.; Hawkins, P.G.; Steiner, J.T.; et al. Lightwave valleytronics in a monolayer of tungsten diselenide. *Nature* **2018**, *557*, 76–80.
38. Xiao, D.; Yao, W.; Niu, Q. Valley–Contrasting Physics in Graphene: Magnetic Moment and Topological Transport. *Phys. Rev. Lett.* **2007**, *99*, 236809.
39. Mak, K.F.; Xiao, D.; Shan, J. Light–valley interactions in 2D semiconductors. *Nat. Photon.* **2018**, *12*, 451–460.
40. Jiménez–Galán, Á.; Silva, R.E.F.; Smirnova, O.; Ivanov, M. Lightwave control of topological properties in 2D materials for sub–cycle and non-resonant valley manipulation. *Nat. Photon.* **2020**, *14*, 728–732.
41. Jiménez–Galán, Á.; Silva, R.E.F.; Smirnova, O.; Ivanov, M. Sub-cycle valleytronics: control of valley polarization using few-cycle linearly polarized pulses. *Optica* **2021**, *8*, 277–280.
42. Sharma, S.; Elliott, P.; Shallcross, S. Valley control by linearly polarized laser pulses: Example of WSe_2. *Optica* **2022**, *9*, 947–952.
43. Golub, L.; Tarasenko, S. Valley polarization induced second harmonic generation in graphene. *Phys. Rev. B* **2014**, *90*, 201402. [CrossRef]
44. Rana, N.; Dixit, G. All–Optical Ultrafast Valley Switching in Two-Dimensional Materials. *Phys. Rev. Appl.* **2023**, *19*, 034056.
45. Mak, K.F.; McGill, K.L.; Park, J.; McEuen, P.L. The valley Hall effect in MoS_2 transistors. *Science* **2014**, *344*, 1489–1492. [CrossRef]
46. Mrudul, M.S.; Jiménez–Galán, Á.; Ivanov, M.; Dixit, G. Light–induced valleytronics in pristine graphene. *Optica* **2021**, *8*, 422–427.
47. He, Y.; Guo, J.; Gao, F.; Liu, X. Dynamical symmetry and valley–selective circularly polarized high–harmonic generation in monolayer molybdenum disulfide. *Phys. Rev. B* **2022**, *105*, 024305.
48. Chen, J.; Liu, C.; Li, R. Valley-Selective Polarization in Twisted Bilayer Graphene Controlled by a Counter-Rotating Bicircular Laser Field. *Photonics* **2023**, *10*, 516.
49. Mrudul, M.S.; Dixit, G. Controlling valley–polarisation in graphene via tailored light pulses. *J. Phys. B At. Mol. Opt. Phys.* **2021**, *54*, 224001.
50. Reich, S.; Maultzsch, J.; Thomsen, C.; Ordejon, P. Tight–binding description of graphene. *Phys. Rev. B* **2002**, *66*, 035412.
51. Jiang, S.; Wei, H.; Chen, J.; Yu, C.; Lu, R.; Lin, C.D. Effect of transition dipole phase on high–order–harmonic generation in solid materials. *Phys. Rev. A* **2017**, *96*, 053850.
52. Dimitrovski, D.; Madsen, L.B.; Pedersen, T.G. High–order harmonic generation from gapped graphene: Perturbative response and transition to nonperturbative regime. *Phys. Rev. B* **2017**, *95*, 035405.
53. Avetissian, H.K.; Avetissian, A.K.; Avchyan, B.R.; Mkrtchian, G.F. Wave mixing and high harmonic generation at two–color multiphoton excitation in two–dimensional hexagonal nanostructures. *Phys. Rev. B* **2019**, *100*, 035434.
54. Avetissian, H.K.; Mkrtchian, G.F.; Knorr, A. Efficient high–harmonic generation in graphene with two–color laser field at orthogonal polarization. *Phys. Rev. B* **2022**, *105*, 195405.
55. Vampa, G.; McDonald, C.R.; Orlando, G.; Klug, D.D.; Corkum, P.B.; Brabec, T. Theoretical Analysis of High-Harmonic Generation in Solids. *Phys. Rev. Lett.* **2014**, *113*, 073901.
56. Liu, X.; Li, L.; Zhu, X.; Huang, T.; Zhang, X.; Wang, D.; Lan, P.; Lu, P. Wavelength dependence of high–order harmonic yields in solids. *Phys. Rev. A* **2018**, *98*, 063419.
57. Zhang, Y.; Li, J.; Li, L.; Huang, T.; Zhu, X.; Lan, P.; Lu, P. Enhancement of the photocurrents injected in gapped graphene by the orthogonally polarized two–color laser field. *Opt. Express* **2021**, *29*, 17387–17397. [PubMed]
58. Vampa, G.; McDonald, C.R.; Orlando, G.; Corkum, P.B.; Brabec, T. Semiclassical analysis of high harmonic generation in bulk crystals. *Phys. Rev. B* **2015**, *91*, 064302. [CrossRef]
59. Guan, Z.; Zhou, X.; Bian, X. High–order–harmonic generation from periodic potentials driven by few-cycle laser pulses. *Phys. Rev. A* **2016**, *93*, 033852. [CrossRef]
60. Wang, H.; Feng, Y.; Fu, S.; Li, J.; Zhang, X.; Du, H. Complex carrier-envelope-phase effect of solid harmonics under nonadiabatic conditions. *Phys. Rev. A* **2019**, *99*, 023406.
61. Liu, X.; Li, Y.; Liu, D.; Zhu, X.; Zhang, X.; Lu, P. Effects of quantum interferences among crystal–momentum–resolved electrons in solid high–order harmonic generation. *Phys. Rev. A* **2021**, *103*, 033104.
62. Zhou, S.Y.; Gweon, G.H.; Fedorov, A.V.; First, P.N.; de Heer, W.A.; Lee, D.H.; Guinea, F.; Castro Neto, A.H.; Lanzara, A. Substrate–induced bandgap opening in epitaxial graphene. *Nat. Mater.* **2007**, *6*, 770–775.
63. Yankowitz, M.; Xue, J.; Cormode, D.; Sanchez-Yamagishi, J.D.; Watanabe, K.; Taniguchi, T.; Jarillo-Herrero, P.; Jacquod, P.; LeRoy, B.J. Emergence of superlattice Dirac points in graphene on hexagonal boron nitride. *Nat. Phys.* **2012**, *8*, 382–386.
64. Grujić, M.M.; Tadić, M.Ž.; Peeters, F.M. Spin-Valley Filtering in Strained Graphene Structures with Artificially Induced Carrier Mass and Spin-Orbit Coupling. *Phys. Rev. Lett.* **2014**, *113*, 046601. [PubMed]
65. Brugnera, L.; Frank, F.; Hoffmann, D.J.; Torres, R.; Siegel, T.; Underwood, J.G.; Springate, E.; Froud, C.; Turcu, E.I.C.; Tisch, J.W.G.; et al. Enhancement of high harmonics generated by field steering of electrons in a two–color orthogonally polarized laser field. *Opt. Lett.* **2010**, *35*, 3994–3996. [PubMed]
66. Cireasa, R.; Boguslavskiy, A.E.; Pons, B.; Wong, M.C.H.; Descamps, D.; Petit, S.; Ruf, H.; Thiré, N.; Ferré, A.; Suarez, J.; et al. Probing molecular chirality on a sub–femtosecond timescale. *Nat. Phys.* **2015**, *11*, 654–658.

67. Smirnova, O.; Mairesse, Y.; Patchkovskii, S. Opportunities for chiral discrimination using high harmonic generation in tailored laser fields. *J. Phys. B At. Mol. Opt. Phys.* **2015**, *48*, 234005.
68. Zhu, X.; Liu, X.; Lan, P.; Wang, D.; Zhang, Q.; Li, W.; Lu, P. Anomalous circular dichroism in high harmonic generation of stereoisomers with two chiral centers. *Opt. Express* **2016**, *24*, 24824–24835.